Recrystallization of a 2D Plasma Crystal

C. A. Knapek, D. Samsonov, S. Zhdanov, U. Konopka, and G. E. Morfill
Max-Planck-Institut für Extraterrestrische Physik, 85740 Garching, Germany
(Received 15 September 2006; published 5 January 2007)

A monolayer plasma crystal consisting of micron-sized particles levitated in the sheath of a rf discharge was melted by applying a short electric pulse to two parallel wires located at the height of the particles. Structural properties and the particle temperature were examined during the stage of recrystallization. A liquidlike phase was followed by a transient state characterized by energy release and the restoring of long range translational order while the defect fraction was low. No long range orientational order was found, though highly ordered domains formed locally. Numerical simulations revealed the same regimes of recrystallization as those observed in the experiment.

DOI: 10.1103/PhysRevLett.98.015004 PACS numbers: 52.27.Lw, 64.60.−i, 64.70.Ja

Phase transitions of two-dimensional systems are a subject of great interest [1–7]. The Kosterlitz-Thouless-Halperin-Nelson-Young theory [8–11] describes a continuous dislocation-mediated melting transition with the appearance of a hexatic phase between the solid and the liquid state and predicts a long range behavior of translational and orientational correlation functions. Plasma crystals [12] provide an ideal opportunity to observe phase transitions of 2D systems at the kinetic level due to the direct visualization of the individual particles and the short restoring time they need to reach equilibrium after a perturbation. Highly charged micron-sized particles in a low temperature electron-ion plasma, interacting via a screened Coulomb potential, are arranged in a single layer crystal. The crystal can be melted by local heating of particles with a laser beam [13] or by application of a strong electric pulse [14]. In this Letter we present the results of a melting experiment with a 2D plasma crystal. The kinetics of the phase transition from the molten state to the crystal is investigated using the particle temperature and structural properties, such as the defect fraction and translational and orientational order parameters. The experimental data are compared with a simulation.

The experiment was performed in a weakly ionized argon plasma generated by a capacitively coupled rf discharge at 13.56 MHz [Fig. 1(a)]. A power of 10 W was applied to the lower horizontal electrode causing a self-bias of −70 V between the electrode and the grounded vacuum chamber. The lower electrode was shaped to create a parabolic potential inside the plasma. The pressure of the argon gas was 1.96 Pa at a flow rate of 4 sccm. This basic setup is similar to that described in Ref. [15]. Two parallel tungsten wires with a diameter of 0.1 mm were mounted horizontally 5.9 mm above the lower electrode and 58.7 mm apart. The wires acquired a negative floating potential in the plasma. Melamine-formaldehyde microspheres with a diameter of 9.19 μm and a mass density of 1.51 g/cm^3 were dispersed into the plasma and gained a high negative equilibrium charge. Because of the electric and gravitational forces they were levitated 4.8 mm above the lower electrode in the plasma sheath and radially confined by the parabolic potential. The mutual interaction between the particles resulted in a two-dimensional hexagonal lattice with a spacing $\Delta \approx 0.6$ mm. Wave spectra analysis as in [16] yielded a particle charge $Q = (13\,000 \pm 1500)e$ and a lattice parameter $\kappa = \Delta/\lambda = 0.8 \pm 0.13$, where λ is the shielding distance. To induce a phase transition, a negative 0.2 s electric pulse of −253 V was applied to the wires. The pulse caused a disturbance, which pushed the particles from both wires to the center of the chamber [as indicated by the arrows on the left of Fig. 1(b)], and melted the crystal [17]. The particles were illuminated with a horizontally spread plane laser sheet of vertical width ≈200 μm provided by a 532 nm Nd:YAG laser. Images were taken with a high speed digital camera from the top at a frame rate of 500 frames/s and a field of view of 1024 × 1024 pixel [outlined by the dashed lines in Fig. 1(b)]. The spatial resolution was 0.034 mm/pixel. Approximately 3400 particles were in the field of view.

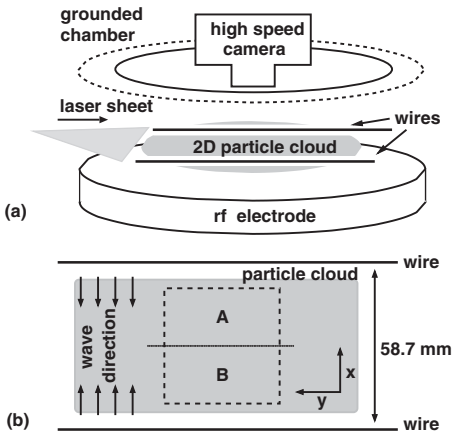

FIG. 1. Sketch of the experimental setup. (a) Oblique view. A monolayer of particles is levitated above the biased electrode and illuminated with a laser sheet. Two parallel wires are mounted 1.1 mm above the particle layer. (b) Schematic top view of the setup. The dashed square outlines the field of view of the camera. The horizontal dotted line denoting the position where the waves from the two wires meet divides the field of view into areas A and B, also used for the temperature analysis.

To reduce the uncertainties in particle positions due to weaker illumination at the image edges, we analyzed only the central part of the images containing ≈ 2300 particles. Particle positions were extracted from the images by an intensity weighting method, and particle velocities were calculated by tracing through consecutive frames. The errors in the particle coordinates $\mathbf{r}$ and the velocities $\mathbf{v}$ due to pixel noise were obtained assuming a Gaussian noise model superimposed on the intensity values of each pixel. The width of this noise distribution was calculated from the fluctuation statistics of the total intensity of individual particle images from one frame to the next. Then the effect on the particle tracking was determined. From this it was concluded that superimposing three consecutive images reduced the errors down to reasonably small values of 0.049 pixel for particle positions and 8.2 pixel/s for velocities.

For each frame the mean particle temperatures T_x, T_y were obtained by using the standard deviations of Maxwellian fits to the velocity histograms of v_x and v_y. The regions A and B in Fig. 1(b) were analyzed separately, since (due to the two oppositely propagating particle motions from both wires to the center) the averaged velocities in these regions have opposite signs shortly after application of the pulse. The standard deviations for both regions were averaged afterwards. The quality of the Maxwellian fit is given by its reduced χ^2, which was on average 3 and 5.8 for regions A and B, respectively, for both v_x and v_y distributions. It was found that T_y is practically always $\approx$ 12% smaller than T_x. This can be understood, since the negative floating potential of the wires compresses the particle layer in the x direction. Note, however, that the common trend, namely, the exponential decay of the particle temperature during recrystallization, is the same for both "transverse" T_x and "longitudinal" T_y components of the total particle temperature. Accordingly, the average value $T = 0.5(T_x + T_y)$ was used (Fig. 2). The exponential decays $\propto e^{-\nu_i t}$ are fitted by solid lines with i indicating four consecutive regimes, numbered from I to IV. In I, $\nu_{\mathrm{I}} = 2.58\ \mathrm{s}^{-1}$, which is close to the Epstein drag coefficient $\nu_{\mathrm{Ep}} = 2.30\ \mathrm{s}^{-1}$ (using [18] with the coefficient for gas drag from [19]); i.e., the particle motion is damped by friction with neutral gas atoms. At $T \approx 1.12$ eV the slope changes to $\nu_{\mathrm{II}} = 1.54\ \mathrm{s}^{-1}$ and at $T \approx 0.52$ eV to $\nu_{\mathrm{III}} = 0.46\ \mathrm{s}^{-1}$. In those regimes some "intrinsic" energy release appears which heats the particles and diminishes the effective cooling rate. In IV the same temperature $T \approx 0.22$ eV as before melting is reached. The cooling rate $\nu_{\mathrm{IV}} \approx 0.025\ \mathrm{s}^{-1}$ is very small and the system is almost equilibrated. The gap between 2 and 4 s corresponds to the time subsequent to the electric pulse where particles moved too fast to be traced sufficiently accurately.

To investigate the structural changes during recrystallization, the pair correlation function $g(r)$, the bond correlation function $g_6(r)$, and the defect statistics were obtained for each frame separately. The pair correlation

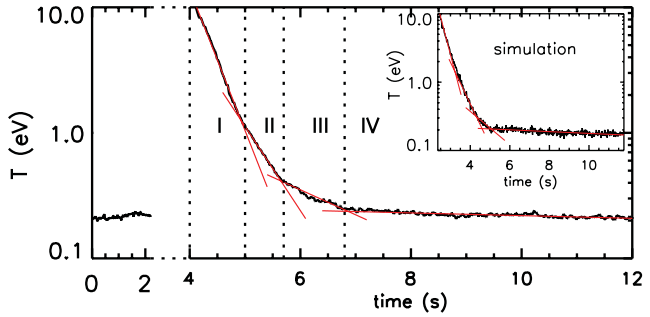

FIG. 2 (color). Mean particle temperature T vs time. Solid red lines correspond to exponential fits in four consecutive regimes with different decays, numbered I to IV (marked by vertical dashed lines). The gap in the time series marks the phase of extremely fast particle motion shortly after the disturbance. Inset: Temperature from simulation. Solid red lines are the same exponentials as those found for the experimental data.

function $g(r)$ gives the probability to find a particle at a distance r away from another one, and is therefore a measure of translational order. In a crystalline state, $g(r)$ should have distinct peaks given by the lattice structure, which are broadened by nonvanishing thermal motion and decay $\propto r^{-\eta(T)}$ with $\eta(T) \leq 1/3$; in hexatic or liquid states, an exponential decay of the peak amplitudes is expected for larger r [20]. The function $g(r)$ was calculated up to distances corresponding at least to $r \approx 17\Delta$. A 3-parameter fit was performed for $g(r)$ with $r \leq 10\Delta$ for each frame using the following function [21]:

$$g_{\mathrm{fit}}(r) = \left[\frac{k}{\sigma}\sum_i g_{\mathrm{id}}(x_i)\exp\left(-\frac{(r-\Delta x_i)^2}{\sigma^2}\right) - 1\right] \times \exp(-r/\xi) + 1,$$

$$\text{with} \quad \sigma = \sigma_0\sqrt{\ln\left(\frac{r}{r_0}\right)}, \qquad r_0 = 0.3\Delta.$$

$g_{\mathrm{id}}(x_i)$ is the value of the pair correlation function of an ideal lattice at the points x_i, and k is a factor depending on the normalization. The fit parameters are the mean interparticle separation Δ, the peak width σ_0, and the correlation length ξ. The fit model was originally derived for crystalline states in [21], but we obtained good agreement with our data up to particle temperatures of 6 eV. For larger temperatures (beginning of regime I in Fig. 2), the above model was used with a constant peak width σ as fit parameter. We also fitted $\sigma_0^2 = KT$ (Fig. 3) as postulated in [21]. We found that indeed $K \approx$ const in the intervals 0.1–0.4, 0.4–2.5, and 2.5–6 eV. However, the values of K differ in these three bands. This suggests that the physics is different in these regimes. The offset of σ_0^2 at $T = 0$ is presumably due to the nonideal lattice structure caused by defects.

The bond correlation function $g_6(r)$ measures the average orientation of nearest neighbor bonds separated by the distance r in the crystal: $g_6(r) = |\frac{1}{N_B}\sum_{l=1}^{N_B}\frac{1}{n(l)} \times \sum_{k=1}^{n(l)}\exp\{i6[\theta(\mathbf{r}_k) - \theta(\mathbf{r}_l)]\}|$, with N_B the total number of

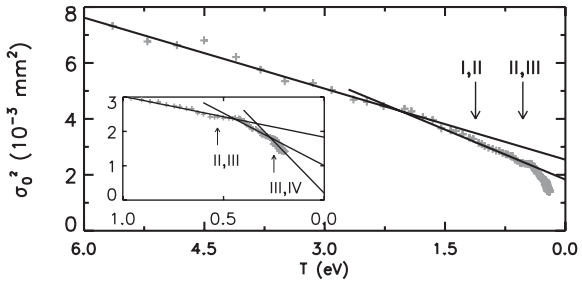

FIG. 3. Squared pair correlation peak width σ_0^2 vs particle temperature. Solid lines are linear fits to three temperature intervals. The arrows indicate the regime borders of Fig. 2. The inset shows a close-up of the temperature range ≤ 1 eV.

bonds in the crystal, $n(l)$ the number of bonds at the distance r from bond l, $\theta(\mathbf{r})$, and respective angles of bonds at $\mathbf{r}$ to an arbitrary axis. The function $g_6(r)$ is constant and close to 1 in the solid state; in the hexatic state for large r a power-law decay $g_6(r) \propto r^{-\eta}$ with $0 \leq \eta \leq 0.25$ is expected, while in the liquid state the decay is exponential $\propto e^{-r/\xi_6}$ with $\xi_6 \leq 4\Delta$ [20]. We fitted exponential decays to $g_6(r)$ for $r \geq 3\Delta$ in the regimes I–IV. In the initial system before melting, a power-law decay was found with an average $\eta = 0.230 \pm 0.004$. This state is not reached after recrystallization in the measurement time.

The parameters ξ/Δ, ξ_6/Δ and the defect fraction are plotted versus time in Figs. 4(a) and 4(b), starting at an offset of 4 s (as for the temperature in Fig. 2). Each data point represents an average over 5 frames. The defects are evaluated for disclinations by calculating the fraction N_k/N of N_k particles with $k = 5$, 7 nearest neighbors; N is the total number of particles. The defect fractions [Fig. 4(a)] decrease linearly in regime I, the decay rate slows down in regimes II and III, and saturations are reached in regime IV where the temperature is practically constant. As shown in Table I, both N_5/N and N_7/N nearly reach their initial values of 1.6%–1.7%. Similar behavior is found for ξ/Δ [red circles in Fig. 4(b)]; for this parameter the initial value $\xi/\Delta \approx 7$ is restored. ξ_6/Δ [blue circles in Fig. 4(b)] increases until $\xi_6/\Delta \approx \xi/\Delta$ is reached at the end of the measurement. A power-law decay of $g_6(r)$ as in the initial state does not occur. Figures 4(c) and 4(d) show the dependence of defect fractions and correlation lengths on the temperature. The regime borders are indicated by arrows. Both defect fractions decrease $\propto T^{0.37}$ during recrystallization [solid line in Fig. 4(c)] in all regimes except the last (crystalline) one. At the border of the crystal regime IV (small T) N_k/N changes abruptly as though the crystal rearranges itself at practically constant temperature. The bond correlation length [Fig. 4(d)] practically doubles in this regime, whereas $\xi/\Delta(T)$ follows roughly a power-law increase $\propto T^{-0.29}$ throughout [solid line in Fig. 4(d)]. One has to remember that the changes in regime IV happen very slowly—amounting to $\approx 65\%$ of the observed recrystallization process.

To investigate the local change of orientational ordering we calculate the sums $\Psi_{6,k} = \frac{1}{n} \sum e^{6i\theta_{kj}}$ over the n nearest

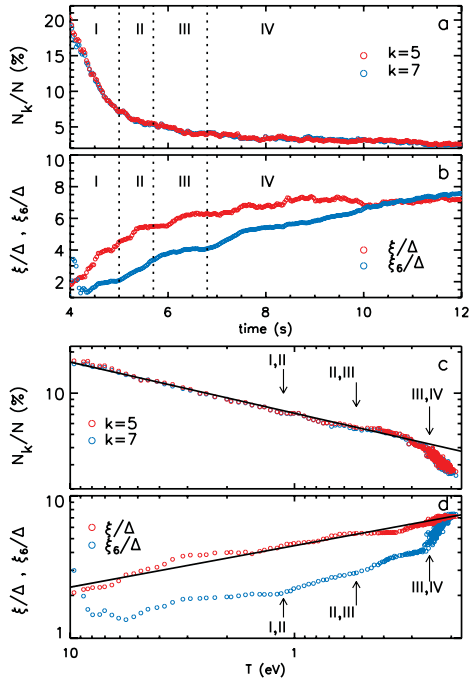

FIG. 4 (color). (a) Defect fractions N_5/N (red) and N_7/N (blue) vs time, and (b) correlation lengths ξ/Δ (red) and ξ_6/Δ (blue) vs time. The dashed lines mark the regimes I–IV of temperature decay. (c) Defect fractions N_5/N (red) and N_7/N (blue) vs temperature. The solid line is $\propto T^{0.37}$. (d) Correlation lengths ξ/Δ (red) and ξ_6/Δ (blue) vs temperature. The solid line is $\propto T^{-0.29}$. The arrows in (c),(d) show the position of the regime borders.

neighbors of each particle k with θ_{kj} being the angle between the nearest neighbor bond of the particles k and j and the x axis in one image. The modulus $|\Psi_{6,k}|$ of this complex quantity gives the bond order parameter [22] which is 1 for an ideal hexagonal structure, whereas the argument $\arg(\Psi_{6,k})$ is a measure for cell orientations with respect to the x axis. Figure 5 shows color-coded maps of $|\Psi_{6,k}|$ for selected frames corresponding to the regimes 0–IV. The arrows represent the vector field of $\Psi_{6,k}$, while the red and blue dots mark the locations of five- and sevenfold defects. The location of bond orientation jumps is clearly correlated with the lines of defect locations. In the initial crystal [Fig. 5(a)] the cells are close

TABLE I. Characteristic quantities of the system. The initial state is numbered 0. During the recrystallization the values at the beginning and end of the observed regimes (Roman numbers I to IV) are given if they differ significantly.

Quantity	Temperature regimes				
	0	I	II	III	IV
T (eV)	0.22	10–1.12	1.12–0.52	0.52–0.24	0.24–0.22
ν (s^{-1})		2.58	1.54	0.46	0.025
N_5/N (%)	1.6	20.1–7.2	7.2–5.4	5.4–3.9	3.9–2.7
N_7/N (%)	1.7	19.5–7.0	7.0–5.3	5.3–4.0	4.0–2.6
ξ/Δ	7	2.1–4.5	4.5–5.4	5.4–6.3	6.3–7.2
ξ_6/Δ		1.2–2.1	2.1–2.9	2.9–4.3	4.3–7.7

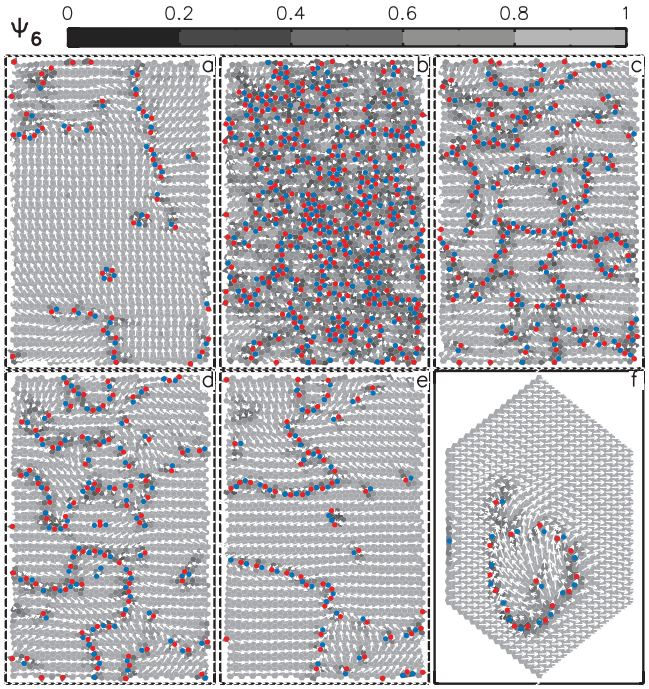

FIG. 5 (color). Color-coded maps of the crystal for different regimes of recrystallization. The background color corresponds to the value of $|\Psi_{6,k}|$ (see colorbar at the top). The arrows represent the vector field of $\arg(\Psi_{6,k})$. Defects are marked by red (fivefold) and blue (sevenfold) dots. (a) Crystal structure before melting (regime 0); (b) liquidlike state immediately after melting (regime I); (c),(d) consecutive regimes II and III of crystallization; (e) metastable regime IV; (f) crystallite structure observed in simulations.

to the ideal hexagonal state and mostly identically oriented [practically no abrupt differences of $\arg(\Psi_{6,k})$ are found]. After melting, a disordered liquidlike state forms [Fig. 5(b)]. Crystallization proceeds first to a system of small ordered ''crystallites'' with arbitrary orientations separated by strings of defects. As the system cools down, these crystallites grow and merge with neighboring regions [Figs. 5(c) and 5(d)], causing the bonds to tilt to the (single) orientation of the growing region. A metastable state is reached which is characterized by highly ordered adjoined crystalline domains [Fig. 5(e)]. Since $\arg(\Psi_{6,k})$ changes abruptly across the domain boundaries—even to directions with opposite signs for adjoining domains—long range orientational order cannot be found in $g_6(r)$ in contrast to the initial state.

A numerical simulation was performed with a hexagonal cluster containing 816 particles at conditions matching those in the experiment. The cluster was heated until a mean particle kinetic energy of 10 eV was reached and then the heating source was switched off. During recrystallization, the system evolved through practically the same exponential temperature decay as in the experiment (see inset of Fig. 2). The formation of a crystallite was observed during the cooling regime [see Fig. 5(f)], also consistent with the results of the experiment.

In conclusion, we investigated the transition of a liquidlike state of a monolayer of particles to a state of high translational order and low defect fraction. The exponential temperature decay changes from pure Epstein damping to a slower decay rate until a constant temperature of 0.22 eV s was reached when defect fraction and translational order are restored to the initial state before melting. Long range orientational order is not present due to the nonuniform orientation of domains across the crystal. It was found that the crystal slowly returns to a more uniform state after a sufficiently long time ($\approx$30 min). The regimes of slow temperature decay (II and III) deserve special attention. We already mentioned that some ''heating'' must occur. This could have two origins—latent heat released by the dissolution of lattice defects and the tilting of nearest neighbor bonds into the (hexagonal) ground state, or the strong coupling between the particles, which would simulate successively larger (more massive) ''unit cells'' or ''effective'' particles.

[1] M. Piech and J. Y. Walz, J. Phys. Chem. B **108**, 9177 (2004).
[2] D. G. A. L. Aarts, M. Schmidt, H. N. Lekkerkerker, and K. R. Mecke, in *Advances in Solid State Physics* (Springer-Verlag, Berlin, 2005), Vol. 45, pp. 15–27.
[3] J. Penfold, Rep. Prog. Phys. **64**, 777 (2001).
[4] H. Kim *et al.*, Phys. Rev. Lett. **90**, 068302 (2003).
[5] T. Baumgart, S. T. Hess, and W. W. Webb, Nature (London) **425**, 821 (2003).
[6] L. Joly, C. Ybert, and L. Bocquet, Phys. Rev. Lett. **96**, 046101 (2006).
[7] E. Lauga and T. M. Squires, Phys. Fluids **17**, 103102 (2005).
[8] J. M. Kosterlitz and D. J. Thouless, J. Phys. C **6**, 1181 (1973).
[9] B. I. Halperin and D. R. Nelson, Phys. Rev. Lett. **41**, 121 (1978).
[10] D. R. Nelson and B. I. Halperin, Phys. Rev. B **19**, 2457 (1979).
[11] A. P. Young, Phys. Rev. B **19**, 1855 (1979).
[12] H. Thomas and G. E. Morfill, Nature (London) **379**, 806 (1996).
[13] V. Nosenko, J. Goree, and A. Piel, Phys. Plasmas **13**, 032106 (2006).
[14] D. Samsonov *et al.*, Phys. Rev. Lett. **92**, 255004 (2004).
[15] S. Nunomura, S. Zhdanov, D. Samsonov, and G. Morfill, Phys. Rev. Lett. **94**, 045001 (2005).
[16] S. Nunomura *et al.*, Phys. Rev. Lett. **89**, 035001 (2002).
[17] Movie at http://www.mpe.mpg.de/~knapek/movies/index.html.
[18] S. Nunomura *et al.*, Phys. Rev. E **65**, 066402 (2002).
[19] B. Liu, J. Goree, V. Nosenko, and L. Boufendi, Phys. Plasmas **10**, 9 (2003).
[20] R. A. Quinn *et al.*, Phys. Rev. E **53**, R2049 (1996).
[21] V. L. Berezinskii, Sov. Phys. JETP **32**, 493 (1971).
[22] D. G. Grier and C. A. Murray, J. Chem. Phys. **100**, 9088 (1994).